Biomolecular surface construction by PDE transform

Qiong Zheng [1], Siyang Yang [1] and Guo-Wei Wei [1,2,*,†]

[1]*Department of Mathematics, Michigan State University, MI 48824, USA*
[2]*Department of Electrical and Computer Engineering, Michigan State University, MI 48824, USA*

SUMMARY

This work proposes a new framework for the surface generation based on the partial differential equation (PDE) transform. The PDE transform has recently been introduced as a general approach for the mode decomposition of images, signals, and data. It relies on the use of arbitrarily high-order PDEs to achieve the time–frequency localization, control the spectral distribution, and regulate the spatial resolution. The present work provides a new variational derivation of high-order PDE transforms. The fast Fourier transform is utilized to accomplish the PDE transform so as to avoid stringent stability constraints in solving high-order PDEs. As a consequence, the time integration of high-order PDEs can be done efficiently with the fast Fourier transform. The present approach is validated with a variety of test examples in two-dimensional and three-dimensional settings. We explore the impact of the PDE transform parameters, such as the PDE order and propagation time, on the quality of resulting surfaces. Additionally, we utilize a set of 10 proteins to compare the computational efficiency of the present surface generation method and a standard approach in Cartesian meshes. Moreover, we analyze the present method by examining some benchmark indicators of biomolecular surface, that is, surface area, surface-enclosed volume, solvation free energy, and surface electrostatic potential. A test set of 13 protein molecules is used in the present investigation. The electrostatic analysis is carried out via the Poisson–Boltzmann equation model. To further demonstrate the utility of the present PDE transform-based surface method, we solve the Poisson–Nernst–Planck equations with a PDE transform surface of a protein. Second-order convergence is observed for the electrostatic potential and concentrations. Finally, to test the capability and efficiency of the present PDE transform-based surface generation method, we apply it to the construction of an excessively large biomolecule, a virus surface capsid. Virus surface morphologies of different resolutions are attained by adjusting the propagation time. Therefore, the present PDE transform provides a multiresolution analysis in the surface visualization. Extensive numerical experiment and comparison with an established surface model indicate that the present PDE transform is a robust, stable, and efficient approach for biomolecular surface generation in Cartesian meshes. Copyright © 2011 John Wiley & Sons, Ltd.

1. INTRODUCTION

The emergence of complexity in self-organizing biological systems poses fabulous challenges to their quantitative description and prediction. The visualization of complex biomolecules, such as proteins, DNAs, molecular motors, and viruses, is of crucial importance to our understanding and conceptualization of biomolecular systems. In particular, the visualization of electrostatic potentials on and around biomolecular surfaces has become an important procedure in the analysis of biomolecular structure, function, and interaction, including ligand–receptor binding, protein specification, drug design, macromolecular assembly, protein-nucleic acid and protein–protein interactions, enzymatic mechanism, and so on. Molecular modeling and visualization have found

---

*Correspondence to: Guo-Wei Wei, Department of Mathematics, Michigan State University, MI 48824, USA.
†E-mail: wei@math.msu.edu

widespread applications in modern science and technologies. In 1953, Corey and Pauling proposed the atom and bond model of molecules, which continues to be a cornerstone in physical science [1]. In crystallography and solid state physics, the regular polyhedral and periodic lattice model is still popular. On the other hand, the molecular and atomic orbital models are important in a quantum mechanical description of molecules and their dynamics. The past few decades have witnessed rapidly increasing interests in biological research. The modeling and visualization of large complex biomolecules have motivated the development of a variety of physical and graphical models.

Under physiological conditions, most biological processes, such as ion channel transport, signal transduction, transcription, and translation, occur in water, which consists of 65%–90% of human cell mass. Physically, the stability and solubility of macromolecules, such as proteins, DNAs, and RNAs, in aqueous environment are determined by how their surfaces interact with solvent, ions, counterions, and/or other surrounding molecules. Therefore, the structure, function, dynamics, and transport of macromolecules depend on the features of their molecule–solvent interfaces [2, 3]. Currently, the van der Waals surface, the solvent-excluded surface (SES) [4], and the solvent-accessible surface are often utilized as molecule–solvent interfaces. In combination with implicit solvent models, these surface models have been applied to protein–protein interactions [5], protein folding [6], protein surface topography [7], drug classification [8], DNA binding and bending [9], macromolecular docking [10], enzyme catalysis [11], solvation energies [12], molecular dynamics [13], and ion channel transport [14–16].

One of the well-known problems associated with the use of van der Waals surface, SES, and solvent-accessible surface is the possibility of having geometric singularities where self-intersecting surfaces and cusps lead to computational difficulties [17–21]. To overcome this difficulty as well as to enforce the important energy minimization principle for any physically stable system, energy variation subject to certain geometric constraint has been adopted as an important approach for the biomolecular surface generation.

To our knowledge, the first partial differential equation (PDE) based construction of biomolecular surface was introduced by Wei and his coworkers in 2005 [22]. Unlike other commonly used PDE-based surface smoothing techniques [23, 24] that start with an existing molecular surface, the PDE-based approach discussed here uses atomic coordinates and radii rather than a given surface to generate hypersurfaces by the time evolution of curvature controlled PDEs, that is, geometric PDEs. The biomolecular surface is subsequently obtained by the isosurface extraction from the hypersurface, or simply called a surface function [22]. This geometric flow approach was originally designed to generate SES type of biomolecular surfaces that are free of geometric singularities.

In 2006, the first variational formulation of biomolecular surfaces based on the surface free energy minimization was introduced [25–27]. The minimal surfaces are omnipresent in nature, such as soap bubbles and oil drops in water. The minimization of surface free energy leads to the mean curvature flow, a PDE whose solution under appropriate constraint gives rise to the minimal molecular surface (MMS) [25–27]. The MMS approach was validated by the calculation of electrostatic solvation free energies of 26 proteins [27]. Our construction and design of the MMS draw upon the experience of our earlier geometric flow approach for biomolecular surface generation [22]. Recently, we proposed a general framework for the construction of biomolecular surfaces by generalized geometric flows in which the surface evolution is determined by the balance of curvature effects and potential effects [28]. This approach enables the incorporation of microscopic interactions, such as van der Waals potentials, into the curvature motion. Based on the aforementioned developments, differential geometry-based multiscale models were introduced by Wei to describe the dynamics and transports of chemical and biological systems, including fuel cells, ion channels, DNA packing, nanofluidic systems, and virus evolution [29]. In these new multiscale models, variational molecular surfaces serve as the solvent–solute interfaces, that separate the atomistic discrete description of macromolecules from the continuum description of the solvent. A total free energy functional is constructed to put the discrete and continuum descriptions, as well as the surface free energy, on an equal footing. The variation of the energy functional via the Euler–Lagrange equation results in coupled Boltzmann equation for electrostatic potential, the generalized Laplace–Beltrami equation for the molecular surface, and other equation for the dynamics of the continuum and/or discrete systems [2, 3, 29].

Recent development in multiscale molecular dynamics [13] calls for fast and reliable surface construction algorithms. During the molecular dynamics simulation, molecular surfaces are repeatedly generated tens of millions of times. Therefore, fast surface construction is crucial to the success of multiscale molecular dynamics. Surface construction is also a key issue in the computation of variational interface-based Poisson–Nernst–Planck (PNP) models [30] and variational interface-based multiscale models for proton transport [31]. A common feature of the aforementioned models is that the surface evolution equation is coupled to other governing equations, for example, the Poisson equation, and thus needs to be solved iteratively and repeatedly for a certain number of times. A main difficulty that slows down the surface construction is that one has to extract embedded geometric information and structure during the solvation analysis. The geometric information and structure can be extremely complex because of the complexity of biomolecular systems [21] and the theoretical model used. Finding geometric feature that preserves fast surface construction remains a challenge in mathematical biophysics.

In the past two decades, there has been a dramatic growth in the research interest of geometric flows [32], particularly mean curvature flows in applied mathematics for image analysis, material design [33–35], and surface processing [23]. In 1983, Witkin introduced the diffusion equation for image denoising [36]. The essential idea of Witkin's algorithm is that the evolution of an image under a diffusion operator is formally equivalent to the standard Gaussian low-pass filter for image denoising. In 1990, Perona and Malik proposed an anisotropic diffusion equation [37], which was designed to remove noise without smearing the image edges. In this approach, the diffusion coefficient depends on the image gradients such that it is small at image edges [37–41]. Computational techniques using the level set formalism were devised by Osher and Sethian [34, 42], and they have aided the success of geometric flows in practical applications. Total variation models were pioneered by Rudin, Osher, and Fatemi [43] for edge-preserving image restoration. The Mumford–Shah variational functional [44] and the Euler–Lagrange formulation of image processing and surface analysis have become popular [43, 45–48].

Both the aforementioned diffusion equation and earlier total variation models are based on the second-order PDEs for image processing or surface analysis. The Willmore flow, proposed in the 1920s, is a fourth-order geometric PDE and has also been used for surface analysis of membranes. In 1999, Wei introduced the first family of arbitrarily high-order nonlinear PDEs for edge-preserving image restoration [39]. The central idea is to accelerate the noise removal by higher-order derivatives. As a variant of Wei's arbitrarily high-order nonlinear PDEs, we also proposed an arbitrarily high-order geometric PDE for molecular surface formation and evolution [28]. Surface generated with such high-order geometric PDE shows a morphology distinguished from that obtained with the second-order PDE. In the past decade, high-order nonlinear PDEs, particularly fourth-order nonlinear PDEs, have attracted much attention in image analysis [28, 39, 41, 49–54]. Unlike the classical second-order PDEs, higher-order PDEs are able to suppress high-frequency components, including noise, at a much faster rate. Mathematical analysis of fourth-order edge-preserving PDEs was carried out by Bertozzi and Greer in Sobolev space [50, 51, 55], proving the existence and uniqueness of the solution to a case with H^1 initial data and a regularized operator. Another analysis by Xu and Zhou [56] was performed under similar conditions. Recently, Jin and Yang have proved the existence of the strong solution of Wei's fourth-order equation, whose mathematical structure differs from other fourth-order PDEs derived from variational formulation [57]. Because high-order PDEs are subject to strict stability constraints in their numerical solutions, computational techniques for higher-order PDEs are important issues, except for digital image processing where the grid size is usually unit. In 2003, Witelski and Bowen designed alternating direction implicit schemes to solve arbitrarily high-order nonlinear PDEs [58].

In early time, both low-order and high-order nonlinear image-processing PDEs are mostly designed to function as low-pass filters. In 2002, Wei and Jia [40] introduced PDE-based band-pass or high-pass filters for image edge detection. The key point of their approach is that when two coupled evolution PDEs are evolving at dramatically different speeds, which is achieved by their largely different diffusion coefficients, the difference of two low-pass PDE operators gives rise to a band-pass filter. The coupling terms are based on the relative fidelity of two images, so as to balance the disparity of two images. One can create a high-pass PDE operator by setting one of the PDE

operator to an identity operator, that is, setting the diffusion and fidelity coefficients to zero, because the difference between an all-pass filter and a low-pass filter is a high-pass filter [40]. Nonlinear PDE-based edge detection operators work extremely well for images with large amount of textures, compared with classical Sobel, Prewitt, and Canny operators [40, 59].

Most recently, we have generalized the nonlinear PDE-based high-pass filter for mode decomposition, that is, the splitting of images, signals, and data into various modes according to their frequency distributions [60–62]. The subsequent processing, or secondary processing, of the individual functional modes thus enables us to achieve our goal of signal, image, surface, and data analysis. Therefore, mode decomposition is a fundamental process in information processing and data analysis [60]. All of the important apparatuses for the PDE-based mode decomposition were developed in our earlier work on arbitrarily high-order PDE filters [39] and PDE-based band-pass or high-pass filters [40]. The process of PDE-based mode decomposition is called a PDE transform because it behaves like the wavelet transform, that is, decomposing data into physically meaningful functional modes and allowing perfect reconstruction. By functional modes, we mean the mode components, which share same band of frequency as well as same category, that is, trend, edge, texture, noise, and so on. Secondary processing of the functional modes obtained by the PDE transform can be applied to achieve various desirable processing tasks such as edge detection, feature extraction, trend estimation, enhancement, denoising, texture analysis, segmentation, and pattern recognition. One of many attractive properties of the PDE transform is its control of time–frequency localization via the order of the PDE transform. Another attractive feature of the PDE transform is its physical space representation. The resulting functional modes are still in the original data form. Because PDE parameters and initial conditions for each individual mode decomposition vary throughout the overall extraction process, the PDE transform is nonlinear process even if a linear PDE is used. In a general sense, PDE transform is the incorporation of the arbitrarily high-order PDE into a recursive mode extraction procedure. In this sense, earlier PDE approaches of image, signal, surface, and data analysis may be regarded as certain special cases.

The objective of the present work is to explore the utility of the PDE transform for fast generation of biomolecular surfaces. We construct a set of arbitrarily high-order nonlinear PDEs by the total variational formulation. These variational PDEs are converted into evolution PDEs by the introduction of an artificial time. To avoid the strict stability constraints of solving high-order PDEs and to gain the desirable acceleration in the surface construction, we make use of the fast Fourier transform (FFT) algorithm to realize the PDE transform in a single time step as in the commonly applied technique [63]. The present algorithm is $O(N \ln N)$. The relations between the order of the PDE transform and molecular surface features, such as surface area, volume, and morphology, have been investigated. Comparison with the existing surface generation algorithms is made. Application to electrostatic potential analysis is carried out by using the Poisson–Boltzmann model and PNP model in which the biomolecular surface is taken as a solvent–solute interface.

This paper is organized as follows. Section 2 is devoted to the theory and formulation of the PDE transform. Apart from describing the basic formalism, a variational derivation is presented. The effects of the order and the propagation time of the PDE transform on surface generation are studied in Section 3. First, two sets of initial values are studied for their performance in the molecular surface generation. We show that biomolecular surfaces constructed from the atomic center Gaussian envelopes do not have desirable smoothness, whereas the present PDE transform-based biomolecular surfaces possess good regularity. The validity of the proposed PDE transform for biomolecular surface generation is explored in Section 4. We examine the computational efficiency as well as surface areas and surface-enclosed volumes of the present method for a large set of proteins. Comparison is given to other established methods in the literature. Furthermore, the application of the proposed approach to protein surface construction is discussed in Section 5. PDE transform-based biomolecular surfaces are further validated and characterized by the solvation free energy analysis via the Poisson–Boltzmann model and by the diffusion analysis via the PNP model. Finally, we consider a challenging application, the construction of virus surfaces, which involves excessively large data sets. The successful applications to these systems indicate the utility of the present PDE transform-based surface generation method. This paper ends with a conclusion of the proposed surface generation techniques.

2. THEORY AND FORMULATION

This section discusses the rationale and variational formulation of the PDE transform. To establish notations and illustrate important concepts, we start by a brief review of high-order PDE-based non-linear low-pass filters introduced by Wei [39]. We construct the PDE transform by the combination of high-order PDEs with an iterative procedure. The performance of the PDE transform depends crucially on the use of high-order PDEs in high-pass or low-pass filters, which gives rise to desired frequency localization. In this section, it is also shown that the PDE transform introduced in our recent work [61, 62] can be derived in variational formula. Fast PDE transform via the fast Fourier analysis is discussed at the end of this section.

2.1. Arbitrarily high-order nonlinear partial differential equations

Although the second-order PDEs are commonly used for image processing and data analysis, the use of high-order PDEs is much less common in practical applications. Motivated by the super flux in the pattern formation in alloys, glasses, polymer, combustion, and biological systems, and the Perona–Malik equation [37], Wei introduced the first family of arbitrarily high-order nonlinear PDEs for image restoration in 1999 [39]

$$\frac{\partial u(\mathbf{r},t)}{\partial t} = \sum_q \nabla \cdot \left[d_q(u(\mathbf{r},t),|\nabla u(\mathbf{r},t)|,t)\nabla\nabla^{2q}u(\mathbf{r},t) \right] + e(u(\mathbf{r},t),|\nabla u(\mathbf{r},t)|,t), \quad q=0,1,2,\ldots$$

(1)

where $\mathbf{r} \in \mathbb{R}^n$, $\nabla = \frac{\partial}{\partial \mathbf{r}}$, $u(\mathbf{r},t)$ is the processed image function, $d_q(u(\mathbf{r},t),|\nabla u(\mathbf{r},t)|,t)$ and $e(u(\mathbf{r},t),|\nabla u(\mathbf{r},t)|,t)$ are inhomogeneous (for example, edge sensitive) diffusion coefficients and enhancement operator, respectively. Equation (1) is subject to the initial data $u(\mathbf{r},0) = X(\mathbf{r})$ and appropriate boundary condition. One can recover the Perona–Malik equation by setting $q = 0$ and $e(u(\mathbf{r}),|\nabla u(\mathbf{r})|,t) = 0$. The fourth-order version of Equation (1) has been applied to image denoising and restoration by many researchers [39, 52, 64, 65].

As in the original Perona–Malik equation, one can choose the hyperdiffusion coefficients $d_q(u(\mathbf{r}),|\nabla u(\mathbf{r})|,t)$ in Equation (1) in many different ways. One popular choice is the Gaussian form

$$d_q(u(\mathbf{r},t),|\nabla u(\mathbf{r},t)|,t) = d_{q0}\exp\left[-\frac{|\nabla u|^2}{2\sigma_q^2}\right],$$

(2)

where the values of constant d_{q0} depend on the noise level. Note that σ_0 and σ_1 are chosen as the local statistical variance of u and ∇u

$$\sigma_q^2(\mathbf{r}) = \overline{|\nabla^q u - \overline{\nabla^q u}|^2} \quad (q=0,1).$$

(3)

The notation $\overline{Y(\mathbf{r})}$ above denotes the local average of $Y(\mathbf{r})$ centered at position $\mathbf{r}$. In this algorithm, the statistical measure based on the local statistical variance is important for discriminating image features from noise. As such, one can bypass the preprocessing of noisy images, that is, the convolution of the noise image with a test function or smooth mask in the application of the PDE operator.

Recently, another family of arbitrarily high-order geometric PDEs has been proposed for surface formation and evolution with application in the surface generation of proteins and other biomolecules [28],

$$\frac{\partial S}{\partial t} = (-1)^q \sqrt{g(|\nabla\nabla^{2q}S|)}\nabla \cdot \left(\frac{\nabla(\nabla^{2q}S)}{\sqrt{g(|\nabla\nabla^{2q}S|)}} \right) + P(S,|\nabla S|),$$

(4)

where S is the hypersurface function, $g(|\nabla\nabla^{2q}S|) = 1 + |\nabla\nabla^{2q}S|^2$ is the generalized Gram determinant and P is a generalized potential term, including microscopic potential effect in biomolecular surface formation. Equation (4) was constructed as a generalization of many other important geometric PDEs. For example, when $q = 0$ and $P = 0$, it reduces to the mean curvature flow equation

used in our earlier formulation of MMSs [28], whereas when $q = 1$ and $P = 0$, it is a surface diffusion flow [28]. Certainly, Equation (4) can also be regarded as a variant of Wei's earlier arbitrarily high-order PDE (1). It is interesting to note that the molecular surface generated by Equation (4) has a distinct morphology [28] although an in-depth analysis has not been presented yet.

Theoretical analysis of high-order nonlinear PDE filtering has always been an important research topic in the applied mathematical community. The well-posedness of Equation (1) was analyzed in terms of the existence and uniqueness of the solution by many researchers [50, 51, 55–57]. Unlike other high-order nonlinear PDEs, Equations (1) and (4) were not derived from a variational formulation. Therefore, mathematical properties of these nonlinear equations differ from those of other high-order PDEs [57].

2.2. Variational formulation of geometric partial differential equations

Variational models are some of the most commonly used approaches in science and engineering. Variational analysis has been an active area of research in applied mathematics [2, 27, 29, 66, 67]. Variational derivation of solvent–solute interfaces has been formulated in many of our recent differential geometry-based multiscale models [2, 3, 29]. Didas *et al.* discussed the variational formulation of high-order nonlinear PDEs [66]. In the present work, we provide alternative expressions for the PDE transform by a variational approach. We define the energy functional as

$$E(u, \nabla u, \nabla^2 u, \ldots, \nabla^m u) = \int \left[\Lambda \left(\sum_{q=1}^{m} |\nabla^q u|^2 \right) + \epsilon (X - u)^2 \right] d\mathbf{r}, \tag{5}$$

where ϵ is a constant, X is the original data, $\epsilon (X - u)^2$ is the fidelity term and $\Lambda(\cdot)$ is an appropriate penalty function. For examples, one can choose many different forms [52, 66]

$$\Lambda(x^2) = x^2 \tag{6}$$

$$\Lambda(x^2) = \left(\sigma^2 + x^2 \right)^{\frac{1}{2}} \tag{7}$$

$$\Lambda(x^2) = e^{x^2/2\sigma^2}, \tag{8}$$

where Equation (6) is the well-known Tikhonov penalty function.

Minimizing the energy functional (5) by the Euler–Lagrange equation, one has

$$\sum_{q=1}^{m} \nabla^q \odot^q \left(\Lambda_{uq} \left(\sum_{q=1}^{m} |\nabla^q u|^2 \right) \nabla^q u \right) + \epsilon (X - u) = 0 \tag{9}$$

where $\odot^q$ is a normal product for even q and an inner product for odd q. Here,

$$\Lambda_{uq}(\cdot) = (-1)^{q+1} \partial \Lambda / \partial \nabla^q u. \tag{10}$$

The energy functional is minimized when Equations (9) are satisfied. To this end, we make use of the steepest descent algorithm with an artificial time and convert Equation (9) into a time-dependent PDE

$$\partial_t u = \sum_{q=1}^{m} \nabla^q \odot^q \left(\Lambda_{uq} \left(\sum_{q=1}^{m} |\nabla^q u|^2 \right) \nabla^q u \right) + \epsilon (X - u) \tag{11}$$

Although the mathematical properties of these nonlinear PDEs may differ from those in Equation (1), Equation (11) is essentially equivalent to the earlier PDE transform [62].

2.3. Partial differential equation transform

One of the important properties of the PDE transform is its ability to extract mode functions from a given data X. One can denote the solution of Equations (1) and/or (11) by $\check{X}(t)$ such that

$$\check{X}^k(\mathbf{r}, t) = \mathcal{L} X^k(\mathbf{r}) \tag{12}$$

where $\mathcal{L}$ is a low-pass PDE transform satisfying $\mathcal{L}u(\mathbf{r}, 0) = u(\mathbf{r}, t)$, $\check{X}^k(\mathbf{r}, t)$ are mode functions and $X^k(\mathbf{r})$ is the kth residue function defined by

$$X^1 = X(\mathbf{r})$$

and

$$X^k = X^1 - \sum_{j=1}^{k-1} \check{X}^j, \quad \forall k = 2, 3, \ldots. \tag{13}$$

Therefore, $X = \sum_{j=1}^{k-1} \check{X}^j + X^k$ is a perfect reconstruction of the original data X in terms of all the mode functions and the final residue. Note that the PDE transform given in Equation (12) recursively generates mode functions based on the input residue function. Obviously, this procedure is nonlinear even if a linear PDE operator is used.

The first mode produced by the present PDE transform is the trend of the data. The residue of the trend is a general edge function. By recursive application of the low-pass PDE transform (12), one can extract all the desired higher-order mode functions. In our earlier work, high-pass PDE transforms were also constructed in which the first mode is edge type of information and the final residue is the trend [61, 62].

2.4. Fast partial differential equation transform

Solving arbitrarily high-order PDEs, such as Equation (1) or (11) in the PDE transform can be a numerically difficult issue for some practical applications. A main concern is the stability constraint as the time stepping size is normally proportional to $2m$th power of spatial grid spacing, where $2m$ is the highest order of the PDE operator. Although one can bypass this difficulty in digital image processing due to unitary spatial grid spacing, the spatial grid spacing is normally smaller than 1 in order to maintain a good resolution in many other applications, including surface construction.

For a linearized form of Equations (1) and (11), we can make use of the Fourier transform to gain computational efficiency. Let us assume a linear PDE of the form

$$\partial_t u = \sum_{j=1}^{m} (-1)^{j+1} d_j \nabla^{2j} u + \epsilon(X^k - u), \quad t \geq 0, \tag{14}$$

where $d_j > 0$, $\epsilon \sim 0$ and $X^k \in \mathbb{R}^n$ is the kth residue of the data. Equation (14) is subject to initial value $u(\mathbf{r}, 0) = X^k$. The exact solution of Equation (14) in the n dimensional Fourier representation is

$$\hat{\check{X}}^k = \hat{\mathcal{L}} \hat{X}^k \tag{15}$$

where $\hat{\check{X}}$ and $\hat{X}^k$ are the Fourier transforms of $\check{X}^k$ and X^k, respectively. Here, $\hat{\mathcal{L}}$ is a frequency response function

$$\hat{\mathcal{L}}(\epsilon, t, d_1, d_2, \ldots, d_m) = e^{-\left(\sum_{j=1}^{m} d_j (w^2)^j + \epsilon\right)t} + \frac{\epsilon}{\sum_{j=1}^{m} d_j (w^2)^j + \epsilon} \left(1 - e^{-\left(\sum_{j=1}^{m} d_j (w^2)^j + \epsilon\right)t}\right), \tag{16}$$

where $w^2 = \sum_{i=1}^{n} w_i^2$.

In the present work, we will also explore the use of the fast PDE transform in the form of Equation (15) for molecular surface generation. Periodic boundary conditions are employed wherever they are necessary.

3. NUMERICAL TESTS

In this section, we validate the proposed PDE transform for surface generation by many numerical tests and experiments. We first discuss two types of initial data used in our evolution PDEs. The suitability of these data for surface construction is examined. With our previous experience,

the highest-order $2m$ of the PDE transform is crucial to its performance. The effect of propagation time t is similar to that of diffusion coefficients d_j, at least for linearized PDEs. Therefore, for simplicity, we set $\epsilon = 0$, $d_j = 0$ $(j = 1, \ldots, m - 1)$ and $d_m = 1$ in all test experiments. The effects of the highest-order $2m$ of the PDE transform and the propagation time t are investigated. Finally, we test the computational efficiency of the proposed method by comparing with the performance of a program for Molecular Surface Computation and Triangulation (MSMS) [20] (http://mgl.scripps.edu/people/sanner/html/msms_home.html).

3.1. Initial data

3.1.1. Piecewise-constant initial values. Piecewise initial data were used in our earlier work for molecular surface construction in the Eulerian representation [22]. For example, in the first PDE-based molecular surface approach, the following initial value was used

$$u(\mathbf{r}, 0) = \begin{cases} 0, & \mathbf{r} \in \bigcup_{\beta=1,\ldots,N_\beta} O(\mathbf{r}_\beta, r_\beta), \\ 1, & \text{otherwise,} \end{cases} \tag{17}$$

that is, if $\mathbf{r}$ lies in any of the sphere $(O(\mathbf{r}_\beta, r_\beta) : \{\mathbf{r} \in \mathbb{R}^3, \|\mathbf{r} - \mathbf{r}_\beta\| \leqslant r_\beta\})$ defined by atomic coordinates, then the value for u is 0, otherwise, $u = 1$. Here, $\mathbf{r}_\beta$ and r_β $(\beta = 1, \ldots, N_\beta)$ are respectively the coordinate and specific radius of each individual atom in the molecule with N_β being the total number of atoms. The atomic specific radius can be chosen as the atomic van der Waals radius.

Note that if the partition of the region labeled by 0 is switched with that labeled by 1, we obtain another alternative non-smooth definition of the initial value, which was extensively used in the generalized Laplace–Beltrami equations in our recent work [2, 27, 28]. Obviously, this type of initial data is not smooth. Its performance for surface generation will be examined.

3.1.2. Gaussian initial values. The Gaussian functions are often used for molecular surface generation. A recent example has been discussed in the literature [21, 68, 69]. Here, we adopt the prescription by Giard and Macq [68] with minor modification as the initial value $u(\mathbf{r}, 0)$

$$u(\mathbf{r}, 0) = \max_\beta \left(s e^{-\frac{\|\mathbf{r} - \mathbf{r}_\beta\|^2 - r_\beta^2}{r_e^2}} \right) \tag{18}$$

where r_e is set to 3 Å and s is the threshold parameter [68]. Obviously, this initial value is more smooth. However, we will show in the next section that molecular surfaces directly extracted from the Gaussian functions can have geometric singularities. It is noted that initial Gaussian values do not directly represent surfaces. Instead, they are functions embedded with surface information.

3.2. Two-dimensional test cases

3.2.1. Effect of the order of the partial differential equation transform. We explore the impact of the order of the PDE transform. Assuming that the propagation time is fixed, the effect of the PDE transform depends on its order $(2m)$. This effect can be analyzed by the Fourier transform. As shown in Figure 1(a), when the propagation time is set to $t = 5000$, as the highest-order $2m$ becomes higher, the frequency response functions provide a wider low-pass window with smooth transition regions. In a two-dimensional (2D) setting, the frequency response functions of a PDE transform are given in Figure 1(b). Obviously, it is a 2D near-ideal low-pass filter.

A 2D initial value formed by three circles is studied to examine the effect of the order $(2m)$ of the PDE transform for the surface formation. The centers of the circles are (-1.8,0), (1.8,0), and (0,3.12), respectively with the same radius 1.8. The initial value $u(r, 0)$ is constructed according to Equation (18) with $N_\beta = 3$. The isosurface at $u(r, 0) = 1.0$ (here, $s = 1.0$) of the initial value is shown in Figure 2(a). The PDE transform is applied to the initial value with $t = 5000$ and five different orders $(2m = 2, 4, 6, 8, 10)$. The frequency responses of PDE transform parameters are shown in Figure 1.
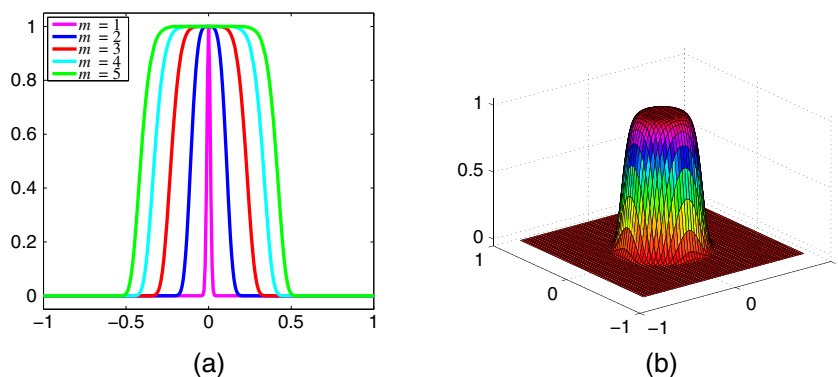
Figure 1. Frequency response functions. (a) 1D frequency response functions obtained at different $2m$ values ($t = 5000$); (b) 2D frequency response function ($2m = 8$ and $t = 5000$).
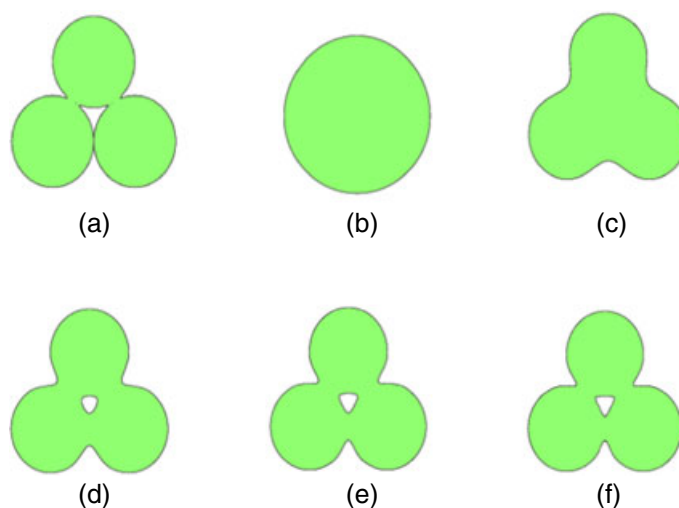

Figure 2. The isosurface of the initial value and isosurfaces obtained from partial differential equation (PDE) transforms of different orders. (a) Initial value, $u(r, t = 5000) = 1.0$; (b) the isosurface after the PDE transform with $2m = 2$, $u(r, t = 5000) = 0.4$; (c) the isosurface after the PDE transform with $2m = 4$, $u(r, t = 5000) = 1.0$; (d) the isosurface after the PDE transform with $2m = 6$, $u(r, t = 5000) = 1.0$; (e) the isosurface after the PDE transform with $2m = 8$, $u(r, t = 5000) = 1.0$; (f). The isosurface after the PDE transform with $2m = 10$, $u(r, t = 5000) = 1.0$.

After the PDE transform, resulting isosurfaces are shown in Figures 2(b–f). It is observed that in subfigure (b), too much information is filtered out and the resulting isosurface differs much from the isosurface of the initial value. In subfigure (c), the resulting isosurface is smooth, without cavity, and also keeps the basic features of the original isosurface. In subfigures (e) and (f), the basic features of the initial isosurface are remained, but the cavity part is not filtered out, and the intersection region of different circles is not so smooth compared with that in subfigure (c). Therefore, the isosurface in Figure 2(c) appears to provide a better result.

To further illustrate the impact of the PDE transform, we provide the Fourier analysis of isosurfaces before and after the PDE transform. As shown in Figure 3(a), the initial value obtained by using Gaussian functions is not smooth at all contours. Therefore, molecular surfaces generated by direct isovalue extraction from Gaussian functions will have potential geometric singularities. The Fourier image of the initial value is given in Figure 3(c). Here, the origin of the frequency domain is at the center of the graph. Obviously, there are many high-frequency components because of the combination of individual Gaussian functions. The goal of the PDE transform is to get rid of high-frequency components. Indeed, after the PDE transform, the high-frequency components
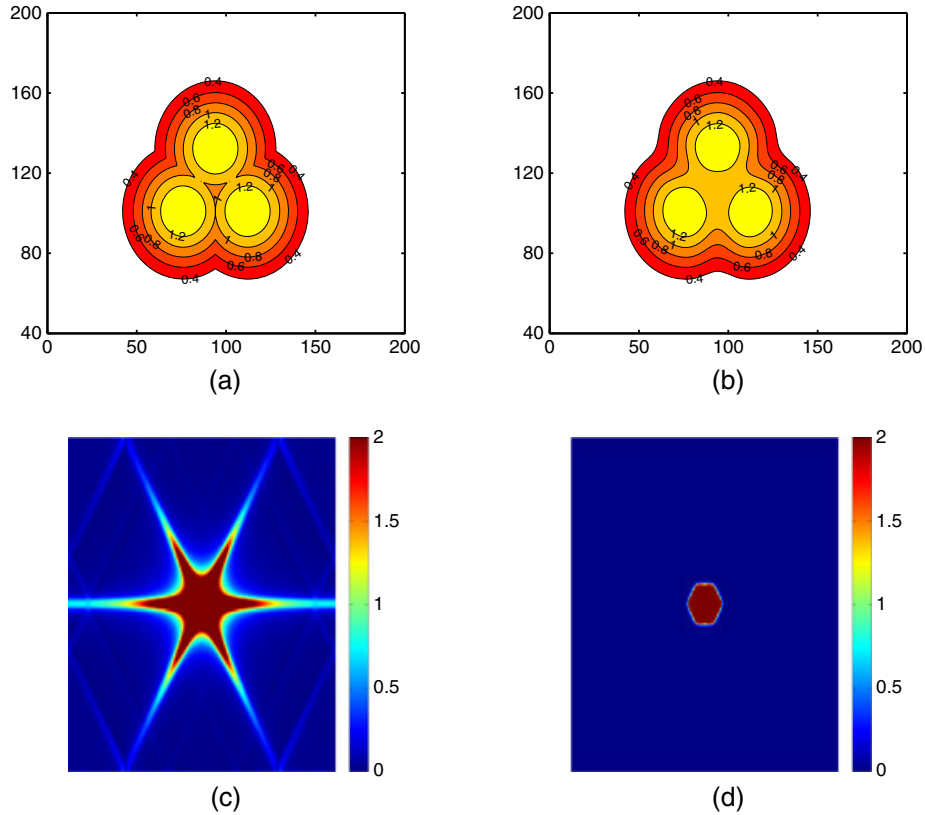
Figure 3. Impact of the partial differential equation (PDE) transform. (a) Initial value shown in the physical domain; (b) isosurface generated by the PDE transform shown in the physical domain. (c) initial value shown in the frequency domain; (d) isosurface generated by the PDE transform shown in the frequency domain; the final isosurface is obtained by taking an isovalue of 1.0.

are effectively reduced as depicted in Figure 3(d). The isosurface generated by the PDE transform is plotted in Figure 3(b). One can obtain a desirable final isosurface by choosing an appropriate isovalue, say 1.0.

3.2.2. Effect of the propagation time of the partial differential equation transform. We next conduct a different test. Assuming that the order of the PDE transform is fixed, then the frequency response function changes with the propagation time. As shown in Figure 4(a), when the order of the PDE
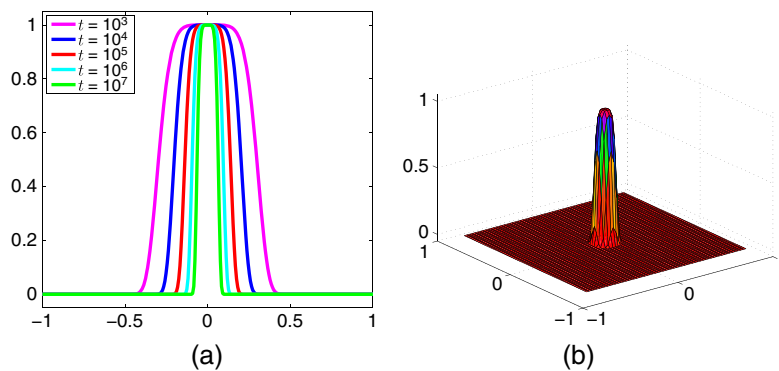

Figure 4. Frequency response functions. (a) 1D frequency response functions obtained at different time t ($2m = 6$); (b) 2D frequency response function ($t = 10^6$ and $2m = 6$).

transform is set to $2m = 6$, as the propagation time t gets longer, the frequency response function provides a smaller low-pass window with smooth transition regions.

The earlier case where surface function is formed by three circles is studied to examine the effect of the propagation time t for the surface formation. Again, the initial isosurface at $u(r, 0) = 1.0$ (here, $S = 1.0$) is shown in Figure 5(a). The PDE transform is applied to the initial value with $2m = 6$ and five different propagation time ($t = 10^3, 10^4, 10^5, 10^6$, and 10^7), where a 1D graph is shown in Figure 4(a) and a 2D illustration is shown in Figure 4(b) with $n = 6$ and $t = 10^6$. One observes near-ideal low-pass filters.

After the PDE transform, resulting isosurfaces given at the same isovalue $u(r, t) = 1.0$ are shown in Figure 5(b–f). It is observed that in subfigures (b) and (c), the intersection corners of different circles are smoothed in different levels, but the cavity part is remained. In subfigures (d–f), the resulting isosurfaces are smooth, without cavity, and also keeps the basic features of the original isosurface. Furthermore, subfigures (d–f) are different in terms of the transition feature. That is, subfigure (f) has lower curvatures compared with (d) and (e) at intersectional regions. Therefore, with an appropriate propagation time, higher-order PDE transforms can also provide desirable computational results in the surface generation. We omit the further test of higher-order PDE transforms. However, in the next section, we demonstrate some practical applications of higher-order PDE transforms for biomolecular surface generations.

3.3. Three-dimensional test cases

In this section, we carry out the PDE transform-based surface generation by embedding the 2D surface in the $\mathbb{R}^3$, namely, an Eulerian representation of 2D surfaces [3]. We first examine appropriate conditions that lead to surfaces with suitable biomolecular morphologies, that is, maintaining biomolecular characteristic, being free of geometric singularities and having a good resolution. Impacts of PDE transform order and propagation time are studied.

All atomic coordinates of proteins are downloaded from the Protein Data Bank (PDB). Atomic van der Waals radii of proteins are adopted from the Chemistry at Harvard Molecular Mechanics (CHARMM) force field [70].

3.3.1. Three-atom test case. We first consider a simple test example: a three-sphere case. The initial atomic coordinates are given as $(0, 0, 1.8)$, $(0, 0, -1.8)$, and $(0, 3.12, 0)$ with a uniform radius of
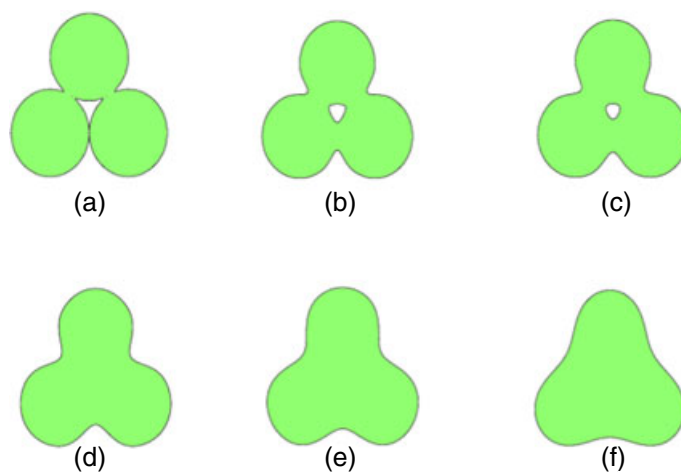

Figure 5. The isosurface of the initial value and isosurfaces $u(r, t) = 1.0$ after partial differential equation (PDE) transforms with $2m = 6$. (a) Initial isosurface; (b) the isosurface after the PDE transform with $t = 10^3$; (c) the isosurface after the PDE transform with $t = 10^4$; (d) the isosurface after the PDE transform with $t = 10^5$; (e) the isosurface after the PDE transform with $t = 10^6$; (f) the isosurface after the PDE transform with $t = 10^7$.

1.8 Å. The effects of the two different sets of initial values presented in Equations (17) and (18) are examined. The Gaussian initial value defined by Equation (18) with the isovalue = 1.0 is shown in Figure 6(a). As in the 2D case, the Gaussian functions lead to geometric singularities in molecular surfaces. As a comparison, the piecewise-constant initial value defined by Equation (17) with the isovalue = 0.6 is shown in Figure 6(d). Obviously, it is a low-quality surface. The surface generated by the PDE transform are presented in Figures 6(b,c,e,f). It is seen that the surfaces generated by using the piecewise-constant initial value have a better quality.

3.3.2. Effects of isovalue and integration time. We carry out our further tests with realistic surface generation of proteins. By choosing a specific protein structure (e.g., PDB ID: 1ajj), the initial value $u(r,0)$ is provided according to Equation (18), and other type of initial values will be examined later. The final surface of the PDE transform is obtained with appropriate isovalues. In Figures 7–9, we plot three surfaces with the propagation time $t = 10^2$, $t = 10^3$, and $t = 10^4$, respectively, and the order of the PDE transform is fixed at $2m = 6$. In these figures, subfigure (a) shows the surface when the isovalue equals 1.0, whereas subfigure (b) depicts the surface when the isovalue equals 0.9.
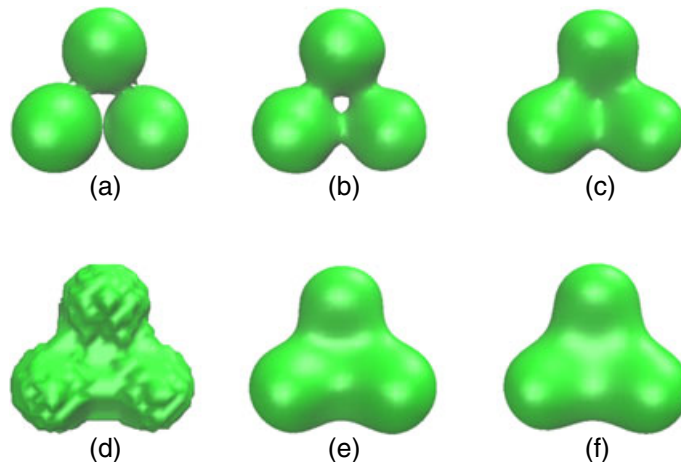

Figure 6. The isosurface of the initial value and isosurfaces ($u(\mathbf{r},t) = 1$ for the first row and $u(\mathbf{r},t) = 0.6$ for the second row) after partial differential equation (PDE) transforms. (a) Initial isosurface defined by Equation (18); (b) the isosurface after the PDE transform with $2m = 12$, $t = 10^4$; (c) the isosurface after the PDE transform with $2m = 12$, $t = 10^6$; (d) initial isosurface defined by Equation (17); (e) the isosurface after the PDE transform with $2m = 12$, $t = 10^4$; (f) the isosurface after the PDE transform with $2m = 12$, $t = 10^6$.
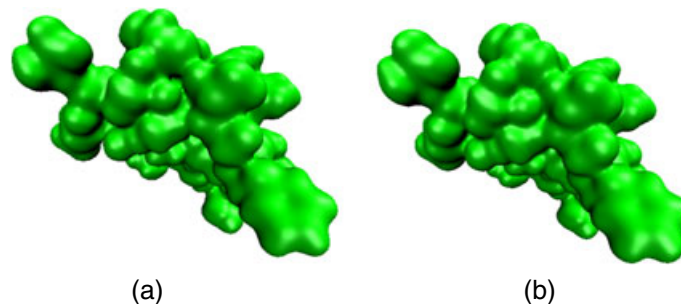

Figure 7. Surfaces of protein 1ajj generated by applying the partial differential equation transform with $2m = 6$ and $t = 10^2$. (a) Isovalue = 1.0; (b) isovalue = 0.9.

Figure 8. Surfaces of protein 1ajj generated by applying the partial differential equation transform with $2m = 6$ and $t = 10^3$. (a) Isovalue $= 1.0$; (b) isovalue $= 0.9$.
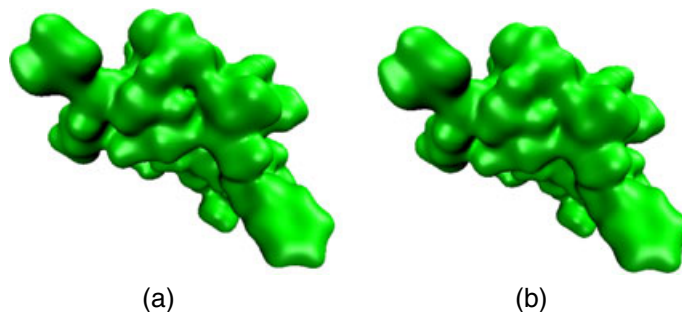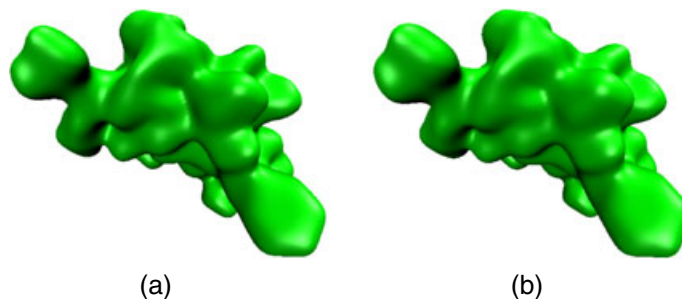

Figure 9. Surfaces of protein 1ajj generated by applying the partial differential equation transform with $2m = 6$ and $t = 10^4$. (a) Isovalue $= 1.0$; (b) isovalue $= 0.9$.

In Figure 7, subfigures (a) and (b) both give good characterizations of the original protein. However, the surface in Figure 7(a) has a cavity that is smaller than the solvent size, which is normally regarded as unphysical. The surface in Figure 7(b) is preferred. For the same reason, the surface in Figure 8(b) is preferred over that in Figure 8(a). Both surfaces in Figure 9(a,b) appear to have been over smeared, if a model is parameterized according to the SES.

Nevertheless, the present PDE transform is able to provide multiresolution representations by controlling the propagation time when the diffusion coefficients are fixed as it is well known that different resolutions can serve different purposes in practical applications. The ability of offering multiresolution surface analysis is a common property for PDE-based methods as originally discussed in our earlier work [22].

In general, a smaller isovalue produces a smoother and more inflated surface. The selection of a surface depends on the parameterization of the theoretical model. For example, some models use solvent-accessible surfaces, whereas other models use solvent-excluded surfaces. For a given protein, the solvent-accessible surface is much more inflated than the solvent-excluded surface. With appropriate parameterizations, one can make both surfaces work well.

3.3.3. Test of piecewise-constant initial values. We now test the piecewise-constant initial values given in Equation (17) for protein surface generation via the PDE transform. After applying the PDE transform with $2m = 12$ and $t = 10^4$, the final surfaces for protein structures (PDB codes: 1ajj and 1hpt) are shown in Figures 10 and 11 with isovalues 0.1 and 0.6. As observed from these figures, subfigures (b) of both figures illustrated much smoother structures comparing with those in subfigures (a) of both figures.

Note that a higher order of the PDE transform is utilized in the present example because piecewise-constant initial values involve many more high-frequency components in their Fourier spectra as illustrated in Figure 3. Therefore, the appropriate use of a higher-order PDE transform can result in a better thresholding of high-frequency components.
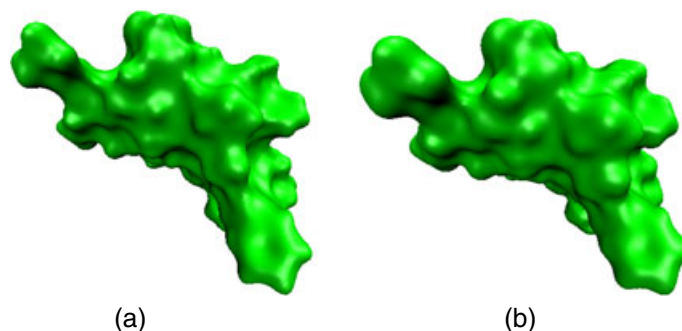
Figure 10. Surfaces of protein 1ajj generated by using the partial differential equation transform with $2m = 12$ and $t = 10^4$. (a) Isovalue = 0.1; (b) isovalue = 0.6.
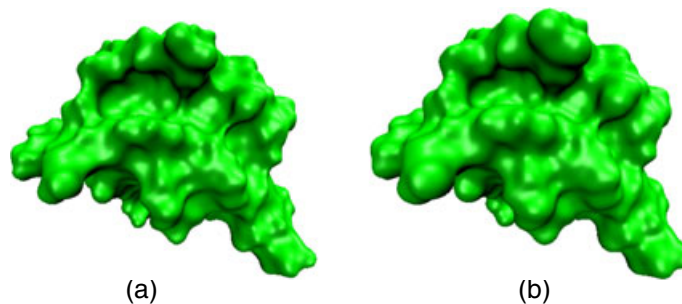

Figure 11. Surfaces of protein 1hpt generated by using the partial differential equation transform with $2m = 12$ and $t = 10^4$. (a) Isovalue = 0.1; (b) isovalue = 0.6.

4. ALGORITHM VALIDATIONS

In this section, we validate the proposed PDE transform method for realistic biomolecular surface generation. We first examine the computational efficiency of the PDE transform for surface generation. As discussed in Section 1, the computational speed is crucial for many dynamical applications, such as Poisson–Boltzmann-based molecular dynamics [13] and coupled nonlinear PNP equations [15, 16]. In fact, surface generation is a major bottleneck in our earlier implicit molecular simulations [13]. In addition, we analyze protein surface area and surface-enclosed volume. These quantities are useful in molecular biology. To ensure the acceptance of the present method by the community, it is important to investigate its consistency with well-established biophysical models in the field. We compare the present results with those of the SES for a large number of protein molecules.

In all computations involving protein structures, atomic coordinates are obtained from the PDB (www.pdb.org). The missing hydrogen atoms are added and point charges at atomic centers are assigned by using the PDB2PQR package—a python-based structural conversion utility [71], based on the CHARMM force field [70]. The initial values for u can be obtained by Equations (17) or (18). Then, the FFT is performed on u by using the fftw software package (www.fftw.org). Therefore, $\hat{u}$ is in the frequency domain, that is, $\hat{u} = \text{FFT}(u)$. Equation (16) is applied to $\hat{u}$, and we denote the updated values as $\hat{\hat{u}}$. Then, the inverse FFT is carried out on $\hat{\hat{u}}$ and $u_{\text{new}} = \text{IFFT}(\hat{\hat{u}})$. The final surface can be extracted from u_{new} by choosing an appropriate isovalue of u_{new}. The computer graphics algorithm, matching cubes, is used to extract the final surface and calculate the surface norm [27].

Whereas the two initial values can be used for the surface generation, we note that, compared with results computed from Gaussian initial values, results from piecewise-constant initial values are more consistent with those of other established methods, such as the SES. In the rest of this paper, the 12th-order PDE transform is used with $t = 10^4$ for all the calculations. The isovalue of 0.6 is used for all the surface extractions. The MSMS package [20] is used to generate SESs. In the

MSMS surface generation, the probe radius is set to 1.4, and the density is chosen as 10, which is equivalent to a Cartesian mesh size of 0.316 Å.

4.1. Computational efficiency

The computational efficiency for the surface generation is important for certain applications, such as molecular dynamics where one needs to repeatedly generate the surface tens of millions of times. The MSMS is known to be very fast in the molecular surface generation. However, the MSMS surfaces are provided in the Lagrangian form, that is, in terms of the triangular surface mesh. In Eulerian computations, the Cartesian mesh is used. Therefore, a Lagrangian to Eulerian conversion, which transfers the surface information from the 2D triangular surface mesh to the 3D Cartesian mesh, is required. This conversion can be very time consuming. In our earlier work, a program for converting the triangular surface mesh to the 3D Cartesian mesh was developed to provide surface information in solving the Poisson–Boltzmann equation [72]. This program is used in the present work. The surface generated by the present PDE transform is directly recorded in the 3D Cartesian mesh. Therefore, no additional Lagrangian to Eulerian conversion is required. Table I provides the details of the CPU time during the whole process of the surface information generation for four different Cartesian mesh sizes: 0.25, 0.5, 0.75, and 1.0 Å. By surface information, we mean three components: identifying points inside and outside the protein, locating and recording the intersection points (the surface points, which intersect with the mesh lines), and extracting the normal direction at each intersection point. In Table I, T_{tot} denotes the time for the surface information generation. For the MSMS approach, T_s represents the time for MSMS surface generation presented in the triangular surface mesh, and T_c represents the time to convert the 2D triangular surface mesh into the 3D Cartesian mesh. The first column of the table shows the PDB codes of proteins as obtained from the PDB bank. Here, N_a is the total number of atoms in the protein, which is counted after the PDB2PQR conversion. The third column lists two different methods, one is based on the PDE transform and the other based on the MSMS approach. The reported CPU time is recorded from a

Table I. Comparison of time efficiency (in seconds) for surface generation in Cartesian meshes by the partial differential equation (PDE) transform and the MSMS approach

PDB ID	N_a	Method	T_s	$h = 0.25$ Å		$h = 0.5$ Å		$h = 0.75$ Å		$h = 1.0$ Å	
				T_c	T_{tot}	T_c	T_{tot}	T_c	T_{tot}	T_c	T_{tot}
1ajj	519	PDE transform			6.52		0.49		0.21		0.10
		MSMS	0.41	6.50	6.91	2.74	3.15	2.70	3.11	2.65	3.06
1bor	832	PDE transform			9.52		0.67		0.23		0.11
		MSMS	0.56	8.54	9.1	4.02	4.58	3.41	3.97	3.42	3.98
1neq	1187	PDE transform			16.29		1.51		0.34		0.14
		MSMS	0.91	12.13	13.04	6.15	7.06	5.95	6.86	5.81	6.72
1a63	2065	PDE transform			18.42		2.21		0.47		0.22
		MSMS	1.31	16.37	17.68	9.03	10.34	8.23	9.54	8.4	9.71
1a7m	2809	PDE transform			24.45		2.72		0.60		0.31
		MSMS	1.73	20.36	22.09	9.83	11.56	8.99	10.72	9.14	10.87
1beb	4972	PDE transform			36.57		5.12		1.04		0.58
		MSMS	2.38	30.1	32.48	18.44	20.82	16.34	18.72	15.92	18.3
1vng	8808	PDE transform			55.29		7.26		2.24		0.96
		MSMS	5.69	46.6	52.29	27.15	32.84	24.71	30.4	22.19	27.88
1a8r	52425	PDE transform			976.86		132.87		36.29		14.62
		MSMS	10.19	NA	NA	NA	NA	NA	NA	NA	NA
1h2i	64460	PDE transform			646.99		91.91		30.66		10.1
		MSMS	19.36*	NA	NA	NA	NA	NA	NA	NA	NA
1gtp	69980	PDE transform			527.56		64.21		19.73		11.79
		MSMS	22.47†	NA	NA	NA	NA	NA	NA	NA	NA

*Surface generated at density 1.454.
†Surface generated at density 1.546.
PDB, Protein Data Bank.

departmental workstation cluster that might be subject to the interruption from jobs submitted by other users during the computation. The MSMS surface generation is essentially a 2D process and depends on the output mesh density. Density 10 is used in the present calculation. It is seen from the table that the MSMS surface generation is very fast compared with the generation by using the PDE transform at finer meshes, which is a 3D processing. However, it takes a major effort to convert the MSMS surface mesh into the 3D Cartesian mesh, which is used in most applications. The surface generation time by using the PDE transform depends crucially on the grid size of the Cartesian mesh. For all proteins tested in the present work, the MSMS approach, including its time for the Lagrangian to Eulerian conversion, is slightly more efficient than the PDE transform at the mesh size of 0.25 Å. However, at a larger mesh size of $h = 0.5$ Å, the PDE transform is generally more efficient than the MSMS approach; at the mesh sizes of $h = 0.75$ and 1.0 Å, the PDE transform is much faster than the MSMS approach. The efficiency of the PDE transform surface generation promises a potential improvement to the molecular dynamics simulation [13].

We also tested some relatively large proteins, namely, 1a8r, 1h2i, and 1gtp that were tested in the literature [68]. In the MSMS surface generation process using probe radius 1.4 Å and density 10, error messages showed up for the 1a8r calculation, and the Lagrangian to Eulerian conversion by using our program [72] was failed. For the MSMS surface generation of 1h2i and 1gtp, no triangular surface data were reported because of error messages and segmentation fault. Alternatively, if one allows the MSMS program to automatically define its density and probe radius parameters, triangular surface meshes could be obtained for 1h2i at a small density of 1.454 and probe radius of 1.5 Å, and for 1gtp at a small density of 1.546 and probe radius of 1.5 Å. However, the Lagrangian to Eulerian conversion still cannot be properly performed because of the poor surface quality. For the PDE transform, the surface generation for these large proteins is stable, and the corresponding CPU time is reported in Table I.

4.2. Surface area and surface-enclosed volume

In this subsection, the quality of the surface generated by the PDE transform is examined through some quantitative studies of surface area and surface-enclosed volume. The performance in these quantitative studies gives an indication of the usefulness of the proposed PDE transform for practical biophysical applications.

To compute surface area and volume in the Eulerian representation, that is, a 2D surface of a biomolecule embedded in a 3D Cartesian grid, we need a numerical algorithm, which is discussed later. The surface integral of a density function $f \in \mathbb{R}^3$ can be evaluated by [13]

$$\int_\Gamma f(x, y, z) dS \approx \sum_{(i,j,k) \in I} \left(f(x_o, y_j, z_k) \frac{|n_x|}{h} + f(x_i, y_o, z_k) \frac{|n_y|}{h} + f(x_i, y_j, z_o) \frac{|n_z|}{h} \right) h^3$$

(19)

where h is the grid spacing size, (x_o, y_j, z_k) is the intersecting point of the interface Γ and the x meshline that passes through (x_i, y_j, z_k), and n_x is the x component of the unit normal vector at (x_o, y_j, z_k). Similar notations are used for y and z directions too. Defining irregular grid points as points with a neighbor from the other side of the interface Γ, I is the set of irregular grid points inside or on the interface [13]. Furthermore, the volume integral of a density function f is approximated by

$$\int_{\Omega_m} f(x, y, z) d\mathbf{r} \approx \frac{1}{2} \left(\sum_{(i,j,k) \in J_1} f(x_i, y_j, z_k) h^3 + \sum_{(i,j,k) \in J_2} f(x_i, y_j, z_k) h^3 \right)$$

(20)

where J_1 is the set of the points inside Ω_m and $J_2 = J_1 \bigcup J_{Irr}$, with J_{Irr} indicating the set of the irregular points. Let $f \equiv 1$; then, Equations (19) and (20) can be applied to compute the surface area and volume, respectively. This approach is second order in accuracy [13].

Table II lists a comparison of surface areas and surface-enclosed volumes for a total of 13 proteins using two types of interfaces: one is constructed by the PDE transform, and the other is generated by using the MSMS package [20]. MSMS package provides SESs in the triangulation form and reports

Table II. Comparison of surface areas, surface-enclosed volumes and electrostatic free energies of solvation for surfaces generated by the PDE transform and the MSMS package. The grid resolution is 0.5 Å.

PDB ID	MSMS surface			PDE transform surface		
	Volume ($\mathring{A}^3$)	Area ($\mathring{A}^2$)	Energy (kcal/mol)	Volume ($\mathring{A}^3$)	Area ($\mathring{A}^2$)	Energy (kcal/mol)
1ajj	4653.4	2166.7	−1136.5	4666.4	2124.5	−1134.1
1bor	7139.1	2898.0	−852.6	7181.9	2832.7	−841.0
2pde	5994.6	2715.9	−820.3	6071.4	2662.1	−807.3
451c	10874.8	4156.3	−1038.6	10917.8	4050.1	−1032.9
1svr	11961.9	4644.0	−1709.7	11979.9	4588.1	−1703.5
1a7m	24025.1	7733.6	−2155.2	24103.9	7524.7	−2135.1
1vii	5050.7	2476.2	−900.4	5084.7	2404.7	−890.0
1vjw	7693.2	2785.8	−1237.3	7618.6	2851.3	−1238.5
1uxc	6791.4	2835.5	−1137.7	6842.0	2785.4	−1129.3
1mbg	7843.3	3070.7	−1348.2	7887.7	2983.7	−1339.9
1ptq	7121.9	2897.4	−872.3	7140.3	2831.6	−870.0
1sh1	6400.7	2743.8	−754.2	6410.7	2683.9	−749.1
1hpt	7660.9	3262.9	−811.1	7699.4	3186.3	−810.1

surface areas and surface-enclosed volumes. It is seen from Table II that surface areas and surface-enclosed volumes generated by these two approaches compare well, which indicates the proposed PDE transform is useful in biophysical applications.

5. APPLICATIONS

As discussed in Section 1, the solvent–solute interface is a crucial element in the implicit solvent models [27, 28], electrostatic calculations [73], solvation analysis [3], molecular dynamics simulations [13], diffusion analysis [15, 16], and differential geometry-based solvation models [29]. Furthermore, it is the starting point to discern biological functions from geometric structures [74]. The surface generation provides the boundary of the protein region, which is defined as the interface between the solvent region and the protein region.

In this section, we apply the PDE transform surfaces to the electrostatic analysis of proteins. The Poisson–Boltzmann model is utilized for this purpose in the present work, although other implicit solvent models, such as generalized Born, can be similarly used. The Poisson–Boltzmann equation reduces to the Poisson equation when there is no ion in the solvent. Electrostatic solvation free energies and electrostatic surface potentials of proteins are evaluated. These properties are important for understanding a wide variety of applications in biophysics and molecular biology. Charge transport analysis is an important approach for a number of applications, including ion channel studies, reaction rate estimation, and binding site specification. We carry out this analysis by applying PDE transform surfaces to the PNP model. Finally, we consider the construction of viral surfaces, which involves an excessively large number of atoms.

5.1. Electrostatic analysis

Once the surface has been generated, the electrostatic potential can be calculated according to the Poisson equation [73, 75, 76]

$$-\nabla\cdot(\epsilon\nabla\phi) = \sum_\beta q_\beta \delta(\mathbf{r} - \mathbf{r}_\beta) \tag{21}$$

where q_β are the (fractional) charges of atoms at position $\mathbf{r}_\beta$ ($\beta = 1, 2, \ldots, N_{\mathrm{a}}$). The dielectric function ϵ is defined as a piecewise constant

$$\epsilon(\mathbf{r}) = \begin{cases} \epsilon_{\mathrm{m}}, & \mathbf{r} \in \Omega_{\mathrm{m}}, \\ \epsilon_{\mathrm{s}}, & \mathbf{r} \in \Omega_{\mathrm{s}}, \end{cases} \tag{22}$$

where $\epsilon_m = 1$ and $\epsilon_s = 80$ are the dielectric constants in the molecular and solvent regions, respectively. Equation (21) is a typical elliptic interface problem with discontinuous coefficients and singular sources, that is, Dirac delta functions. It is very difficult to construct second-order convergent methods for this equation in the biomolecular context because of the geometric complexity, non-smooth interface, and singular charge sources [73, 75, 76].

To remove the Dirac delta functions, Green's function formulation is employed [73]. In this approach, one splits ϕ into the regular part $\widetilde{\phi}(\mathbf{r})$ and the singular part $\overline{\phi}(\mathbf{r})$, that is, $\phi = \widetilde{\phi} + \overline{\phi}$, where $\overline{\phi}(\mathbf{r})$ is defined only in Ω_m [73, 77]. The singular part can be further written as the sum of two terms, $\overline{\phi}(\mathbf{r}) = \phi^*(\mathbf{r}) + \phi^0(\mathbf{r})$.

The first term $\phi^*(\mathbf{r})$ is Green's function, which can be analytically written as

$$\phi^*(\mathbf{r}) = \frac{1}{4\pi} \sum_{\beta=1}^{N_\beta} \frac{q_\beta}{\epsilon_m \mid \mathbf{r} - \mathbf{r}_\beta \mid}. \tag{23}$$

To compensate the values induced by Green's function ϕ^* on the interface Γ, the second term $\phi^0(\mathbf{r})$ satisfies the following Laplace equation with a Dirichlet boundary condition

$$\begin{cases} \nabla^2 \phi^0(\mathbf{r}) = 0, & \mathbf{r} \in \Omega_m \\ \phi^0(\mathbf{r}) = -\phi^*(\mathbf{r}), & \mathbf{r} \in \Gamma. \end{cases} \tag{24}$$

The regular part $\widetilde{\phi}$ of the electrostatic potential satisfies the homogeneous Poisson equation with a modified Neumann condition at the biomolecular interface [73].

$$\begin{cases} -\nabla \cdot (\epsilon \nabla \widetilde{\phi}(\mathbf{r})) = 0 & \mathbf{r} \in \Omega \\ [\widetilde{\phi}(\mathbf{r})] = 0 & \mathbf{r} \in \Gamma \\ [\epsilon \widetilde{\phi}_\mathbf{n}(\mathbf{r})] = \epsilon_m \nabla(\phi^*(\mathbf{r}) + \phi^0(\mathbf{r})) \cdot \mathbf{n} & \mathbf{r} \in \Gamma \end{cases} \tag{25}$$

In this work, we use the matched interface and boundary (MIB) method [75, 78–82] to solve Equation (25). The solution of the Poisson equation can be used for the calculation of electrostatic solvation free energies and for the analysis of electrostatic surface potentials. In the following contents, the electrostatic potential is computed in units of $k_B T / e_c$, and the energy is in units of kcal/mol.

5.1.1. Electrostatic solvation free energy. By definition, the solvation free energy is obtained by

$$\Delta G = \frac{1}{2} \sum_\beta q_\beta (\phi(r_\beta) - \phi_{\text{homo}}(r_\beta)), \tag{26}$$

where ϕ and ϕ_{homo} correspond to the electrostatic potentials in the inhomogeneous and homogeneous environments, respectively. With the decomposition of ϕ, the solvation energy can be calculated by [73]

$$\Delta G = \frac{1}{2} \sum_\beta q_\beta (\widetilde{\phi}(r_\beta) + \phi^0(r_\beta)). \tag{27}$$

The MIB method is used for computing the electrostatics potential values and the electrostatic solvation free energy based on MSMS surfaces. The corresponding results are also shown in Table II. From the table, it is seen that the surfaces generated by the PDE transform lead to similar results comparing to those of the surfaces generated by the MSMS. Moreover, it can be noticed that surface volumes are slightly larger for those of PDE transform surfaces, which results in relatively smaller (in magnitude) electrostatic solvation free energies.

Electrostatic surface potential

We next consider the electrostatic surface potential, which is useful in the understanding of protein–protein interaction, drug design target, DNA specification, and so on. We compute the electrostatic potential by solving the Poisson equation and map the potential on a surface with the VMD software package. Two protein molecules, 1svr and 1a7m, are selected in our analysis. Our results are compared with those of the MSMS surfaces. As shown in Table II, for each of these two proteins, the electrostatic free energies of two surfaces agree very well. It can be seen from Figures 12 and 13 that surface electrostatic potentials produced by two surface models give a very good match too. However, visually, the surfaces generated by the present PDE transform appear to be more smooth and have more reasonable morphologies. Specifically, as shown in Figure 13(a), there is a sharp tip in the cavity region of the SES, whereas, as shown in Figure 13(b), the PDE transform surface does not create unphysical geometric singularities.

5.2. Charge transport analysis

Charge transport phenomena are extremely common in nano-bio systems. In many continuum models and multiscale models, the computational domain is separated into different subdomains with different physics and governing equations. One major role for the biomolecular surfaces is to define the boundary of the solute region or ion exclusion region, that is, the interface between the solvent and solute regions. Here, we devise the surfaces generated by PDE transform for charge transport analysis.

One of the most popular models is the PNP equations, which has a wide variety of applications, including ion channel system, electrochemical diffusion, and so on. The PNP model employs
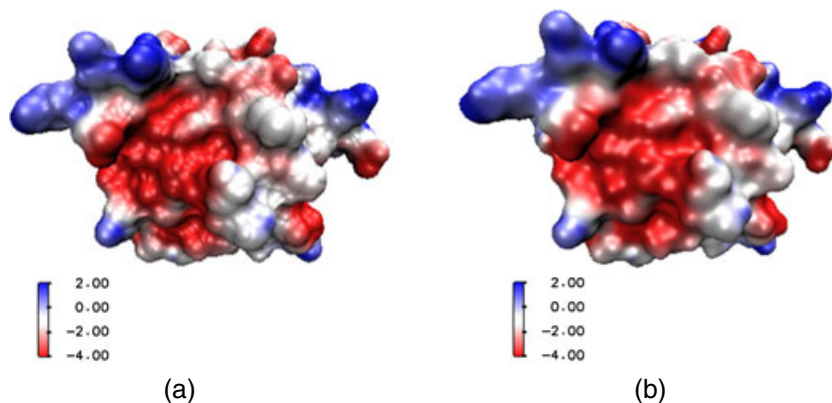

(a)   (b)

Figure 12. Electrostatic surface potentials for protein 1svr mapped on two surfaces. (a) Surface generated by MSMS; (b) surface generated by the 12th-order partial differential equation transform.

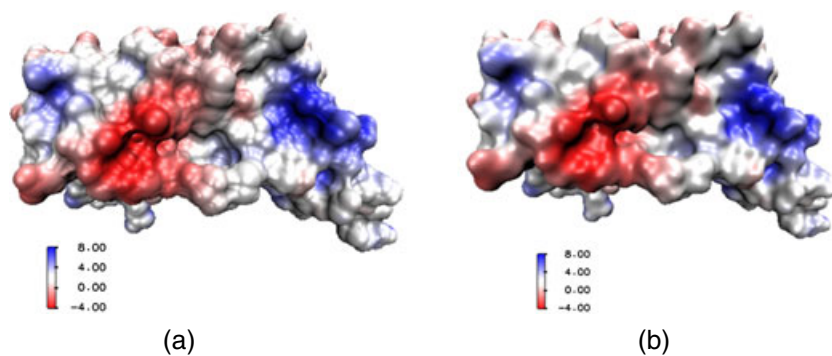(a)   (b)

Figure 13. Electrostatic surface potentials for protein 1a7m mapped on two surfaces. (a) Surface generated by MSMS; (b) surface generated by the 12th-order partial differential equation transform.

the mean-field theory for describing the electrostatic potential via the Poisson equation and the Nernst–Planck theory description of electrodiffusion of ions in the biological environment. We utilize PDE transform surfaces to describe the interface between a solvent and a biomolecule. The electrostatic potential profile $\Phi(\mathbf{r})$ is determined by the Poisson equation

$$-\nabla\cdot(\epsilon(\mathbf{r})\nabla\Phi(\mathbf{r})) = \sum_{\beta=1}^{N_{\mathrm{a}}} q_\beta \delta(\mathbf{r}-\mathbf{r}_\beta) + \sum_{\alpha=1}^{N_{\mathrm{c}}} q_\alpha C_\alpha(\mathbf{r}), \tag{28}$$

where q_β is the (fractional) charge of the protein at position $\mathbf{r}_\beta$ ($\beta = 1, 2, \ldots, N_{\mathrm{a}}$), q_α and C_α are respectively the charge and concentration of the αth ionic species ($\alpha = 1, 2, \ldots, N_{\mathrm{c}}$). Constants N_{a} and N_{c} are the number of charged atoms in the biomolecule and the number of ionic species in the solvent, respectively. The Nernst–Planck equation describes the rate of change of the concentration of each ion species due to the concentration flux

$$\frac{\partial C_\alpha(\mathbf{r})}{\partial t} = -\nabla \cdot \mathbf{J}_\alpha(\mathbf{r}), \tag{29}$$

where the concentration flux is defined by

$$\mathbf{J}_\alpha(\mathbf{r}) = -D_\alpha(\mathbf{r})\left[\nabla C_\alpha(\mathbf{r}) + \frac{q_\alpha}{k_{\mathrm{B}}T} C_\alpha(\mathbf{r})\nabla\Phi(\mathbf{r})\right]. \tag{30}$$

Here, constants k_{B} and T are, respectively, the Boltzmann constant and the absolute temperature, $D_\alpha(\mathbf{r})$ is the spatially dependent diffusion coefficient of species α.

On the interface Γ, the Poisson equation (28) satisfies the jump conditions

$$\begin{cases} [\Phi(\mathbf{r})] = \Phi^{\mathrm{m}}(\mathbf{r}) - \Phi^{\mathrm{s}}(\mathbf{r}) = 0, & \mathbf{r} \in \Gamma, \\ [\epsilon(\mathbf{r})\Phi_{\mathbf{n}}(\mathbf{r})] = \epsilon_{\mathrm{m}}\nabla\Phi^{\mathrm{m}}(\mathbf{r})\cdot\mathbf{n} - \epsilon_{\mathrm{s}}\nabla\Phi^{\mathrm{s}}(\mathbf{r})\cdot\mathbf{n} = 0, & \mathbf{r} \in \Gamma, \end{cases} \tag{31}$$

where ϵ_{m} and ϵ_{s} are the dielectric functions in the molecular and solvent regions; the superscripts in Φ^{m} and Φ^{s} indicate that Φ is defined in Ω_{m} and Φ is defined in Ω_{s}, respectively; and $\mathbf{n} = (n_1, n_2, n_3)$ is the outward normal direction of the interface. Physically there is no ion penetration through the interface Γ, one simply requires that the flux vanishes on Γ, that is

$$-D_\alpha(\mathbf{r})\left[\nabla C_\alpha(\mathbf{r}) + \frac{q_\alpha}{k_{\mathrm{B}}T} C_\alpha(\mathbf{r})\nabla\Phi(\mathbf{r})\right] = \mathbf{0} \text{ on } \Gamma. \tag{32}$$

As observed from Equations (31) and (32), the implementation relies on the definition of the interface Γ. The PDE transform surface serves as the interface Γ during the solution of the PNP equation.

Based on the MIB technique, we have developed a second-order convergent algorithm for solving the PNP equations [15]. Here, we utilize this algorithm and the surface generated by the PDE transform to compute the electrostatic potential and concentration profiles of protein 1ajj. To test accuracy, we have designed analytical test solutions for the PNP equations with biomolecular surfaces [15]

$$\Phi(\mathbf{r}) = \begin{cases} \cos x \cos y \cos z + \phi^*(\mathbf{r}) & \mathbf{r} \in \Omega_{\mathrm{m}} \\ -\dfrac{0.4\pi}{3\epsilon_{\mathrm{s}}}\cos x \cos y \cos z & \mathbf{r} \in \Omega_{\mathrm{s}} \end{cases} \tag{33}$$

$$C_1(\mathbf{r}) = \begin{cases} 0 & \mathbf{r} \in \Omega_{\mathrm{m}} \\ 0.2\cos x \cos y \cos z + 0.3 & \mathbf{r} \in \Omega_{\mathrm{s}} \end{cases} \tag{34}$$

$$C_2(\mathbf{r}) = \begin{cases} 0 & \mathbf{r} \in \Omega_{\mathrm{m}} \\ 0.1\cos x \cos y \cos z + 0.3 & \mathbf{r} \in \Omega_{\mathrm{s}} \end{cases} \tag{35}$$

where ϕ^* is given by Equation (23) with all point charges from the CHARMM force field of protein 1ajj.

Errors of our calculation are listed in Table III. Second-order convergence is observed in both L_∞ norm and L_2 norm, which serves as an indication of good surface quality. At equilibrium, the electrostatic potential computed with the PNP equations is similar to that obtained with the Poisson–Boltzmann model [16]. In the present case, it is given by Equation (33). Therefore, we refrain from offering its illustration.

5.3. Virus surface generation

Surface generation of excessively large biomolecules, such as viruses, is relatively difficult. Recently, we have developed the geometric flow approach for viral surface construction [83]. In the present work, we apply our PDE transform method for viral surface generation.

Viral surfaces usually contain from tens of thousands to tens of millions of atoms, depending on viral species. Many viruses make use of symmetry to reduce genome size and increase stability. The same symmetry can be utilized to reduce the data size during the surface construction. To further reduce the data size, one can make use of coarse-grained models, in which each amino acid can be represented by one or a few super-atoms [83]. These techniques are also employed in the present study.

We consider the rice yellow mottle virus, a major pathogen that dramatically reduces rice production in many African countries. Its structure has an icosahedral symmetry. Its atomic coordinates are obtained from the PDB (ID: 1f2n) [84]. With the surface patch generated by the PDE transform, we compute its unit normal direction as $\frac{\nabla u}{\|\nabla u\|}$, where u is a surface function [3], by using the points on the surface, which intersects with the mesh lines. Then, according to the symmetric information recorded in the PDB file, the surface patch is extended to the whole virus domain. We have generated virus surface patches with three propagation lengths, that is, $t = 10^4, t = 10^5$, and $t = 10^6$, and the resulting virus surfaces are shown in Figure 14(b–d). It is interesting to note that these virus surfaces demonstrate different resolutions of the same virus. Therefore, our PDE transform is able to provide a multiresolution analysis in surface visualization. As a comparison, one of the VMD representations is illustrated in Figure 14(a).

6. CONCLUDING REMARKS

Mode decomposition is an elementary task in signal and image processing. A new approach, PDE transform, has been proposed recently for mode decomposition [61, 62]. Like the wavelet transform, the PDE transform is able to decompose signal, image, and data into intrinsic modes and functional modes, such as trend, texture, edge, noise, and feature. Additionally, the PDE transform makes use of arbitrarily high-order PDEs to achieve the desirable time–frequency localization and tunable frequency precision in a very robust way. In the present work, we explore the use of the PDE transform for the generation of biomolecular surfaces, which are crucial components in the implicit

Table III. Numerical errors in solving Poisson–Nernst–Planck equations for surfaces of protein 1ajj.

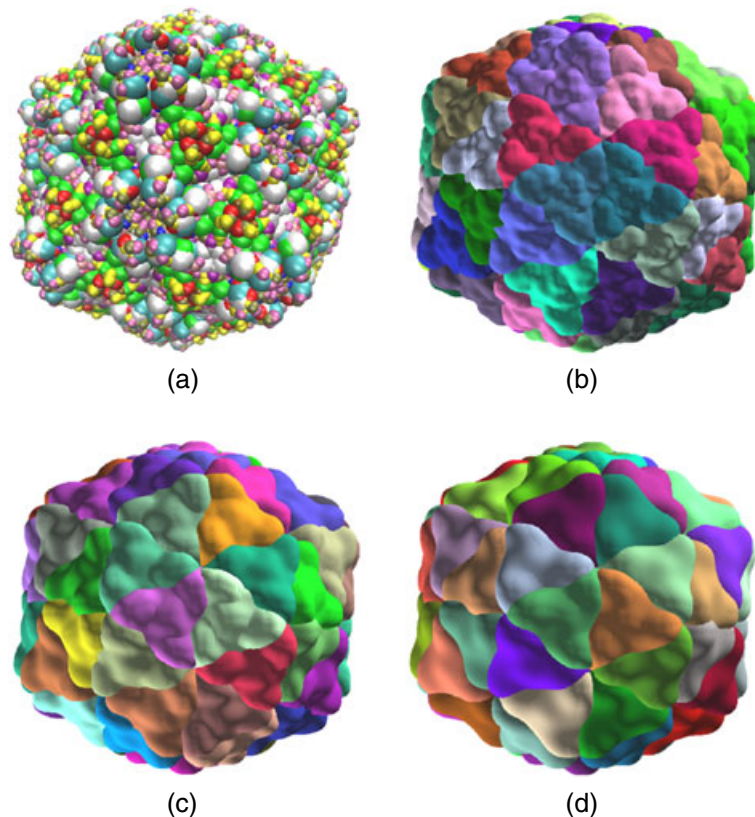|	Mesh size (Å)	Numerical errors			
		L_∞	L_∞ order	L_2	L_2 order
	$h = 1.0$	9.43E-002	—	6.43E-003	—
Φ	$h = 0.5$	2.34E-002	2.0107	1.59E-003	2.0158
	$h = 0.25$	5.95E-003	1.9755	3.99E-004	1.9946
	$h = 1.0$	6.16E-002	—	6.10E-003	—
C_1	$h = 0.5$	8.19E-003	2.9110	1.44E-003	2.0827
	$h = 0.25$	2.02E-003	2.0195	3.54E-004	2.0242
	$h = 1.0$	3.50E-002	—	3.29E-003	—
C_2	$h = 0.5$	5.14E-003	2.7675	7.59E-004	2.1159
	$h = 0.25$	1.14E-003	2.1727	1.84E-004	2.0444

Figure 14. Surfaces of virus 1f2n. (a) VMD surface constructed via symmetry (colors indicate amino acid residues); (b) partial differential equation (PDE) transform surface constructed via symmetry ($t = 10^4, 2m = 6$, colors indicate symmetric elements); (c) PDE transform surface constructed via symmetry ($t = 10^5, 2m = 6$, colors indicate symmetric elements); (d) PDE transform surface constructed via symmetry ($t = 10^6, 2m = 6$, colors indicate symmetric elements).

solvent models [73], charge transport models [15], and differential geometry-based multiscale models [29] for biomolecular systems. These models have a wide variety of applications in biophysics and molecular biology.

We first give a different derivation of the total variational formulation of the arbitrarily high-order PDEs. Additionally, we propose an FFT algorithm to implement the present PDE transform for surface construction. Moreover, we consider two types of initial values, ones generated by using Gaussian functions and ones by using piecewise constants. We found that although both initial values work well, the piecewise-constant initial values deliver better results. It is noticed that biomolecular surfaces generated via a direct isosurface extraction from Gaussian functions-located atomic centers may have a very low regularity. Consequently, they may not be suitable for surface meshing and biophysical applications. Further, we examine the impact of PDE orders in the PDE transform on the surface morphology. It is found that high-order PDE transforms are very useful in surface generations. We also test the effect of the PDE integration time on the surface formation. A proper combination of the PDE order and integration time is required to deliver good-quality surfaces, which maintain biomolecular traits, are free of geometric singularities, and have a good resolution. Furthermore, we validate the proposed method by computational efficiency and quantitative analysis of surface areas and surface-enclosed volumes of a set of test proteins. Finally, the present surface generation approach is applied to a number of problems.

In the validation analysis, biomolecular surfaces of 13 proteins are generated by using the PDE transform. Quantitative analysis is carried out on the surface areas and surface-enclosed volumes

in the present study. As an additional validation, we have compared our results with those of an established method, the SES [4] implemented by the MSMS package [20]. Very good consistency is observed. We choose a set of 10 proteins to test computational efficiency for the surface generation in the Cartesian mesh. The present surface generation method is more efficient than the MSMS approach at mesh sizes larger than 0.5 Å, whereas less efficient at mesh sizes less than 0.25 Å. The present method is more stable than the MSMS approach for proteins of tens of thousands atoms. To further validate the proposed PDE transform approach for biomolecular surface construction, we considered electrostatic solvation analysis via the Poisson–Boltzmann model. Electrostatic solvation free energies of 13 proteins are computed with the Poisson equation model based on our new surfaces. Our results compare well with those of SESs. Electrostatic surface potentials are mapped on to our new surfaces. Compared with surfaces generated by the MSMS, the PDE transform surfaces have better visual effects for electrostatic surface potentials. In another application, we have solved the PNP equations defined on our PDE transform surface of protein 1ajj. Second-order convergent numerical methods based on MIB are utilized in computation. Finally, we have demonstrate the ability of the proposed method for the surface construction of excessively large biomolecules, namely viral capsids. Both coarse-graining and symmetry techniques are utilized to reduce data size and improve the computational capability. We show that the present PDE transform has the ability to offer a multiresolution analysis in virus surface visualization. Our extensive numerical validation and application indicate that the proposed PDE transform offers a feasible, robust, and efficient new approach for the construction of macromolecular surfaces.

Whereas our previous work on the molecular surface generation [27, 28] relies on the second-order nonlinear PDE and the surface evolution is subject to the constraint of the VDW surface, the present work explores the impact of high-order PDEs on the surface generation, and the surface evolution starts from the VDW surface embedded in 3D Cartesian meshes without any constraints. Consequently, the high-order linear PDEs are solved by using the FFT, which leads to computational efficiency. In fact, previous nonlinear PDE methods are able to embed geometric information such that the MMS can be created [27]. In contrast, the present approach based on the FFT does not preserve geometric information, although other computational techniques might be resorted to enforce the geometric constraint. However, we anticipate computational difficulty in the implementation of high-order nonlinear PDE transform.

The present PDE transform-based surface generation has a few special features. One feature of the present approach is that it makes use of the FFT to realize direct time integration of high-order PDEs. Another feature of the present approach is that the resulting surfaces are given in the Cartesian representation, which is convenient for subsequent electrostatic analysis by using the Poisson–Boltzmann equation or the charge transport evaluation by using the PNP equations. The other feature of the present approach is that the resulting biomolecular surfaces are of high regularity and free of geometric singularities. Finally, multiresolution representations of a surface can be achieved by adjusting the PDE propagation time with fixed diffusion coefficients.

REFERENCES

1. Corey RB, Pauling L. Molecular models of amino acids, peptides and proteins. *Review of Scientific Instruments* 1953; **24**:621–627.
2. Chen Z, Baker NA, Wei GW. Differential geometry based solvation models I: Eulerian formulation. *Journal of Computational Physics* 2010; **229**:8231–8258.
3. Chen Z, Baker NA, Wei GW. Differential geometry based solvation models II: Lagrangian formulation. *Journal of Mathematical Biology* 2011. DOI: 10.1007/s00285-011-0402-z.
4. Richards FM. Areas, volumes, packing, and protein structure. *Annual Review of Biophysics and Bioengineering* 1977; **6**(1):151–176.
5. Crowley P, Golovin A. Cation-pi interactions in protein–protein interfaces. *Proteins: Structure, Function, and Bioinformatics* 2005; **59**:231–239.

6. Spolar RS, Record Jr MT. Coupling of local folding to site-specific binding of proteins to DNA. *Science* 1994; **263**:777–784.
7. Kuhn L, Siani MA, Pique ME, Fisher CL, Getzoff ED, Tainer JA. The interdependence of protein surface topography and bound water molecules revealed by surface accessibility and fractal density measures. *Journal of Molecular Biology* 1992; **228**:13–22.
8. Bergstrom C, Strafford M, Lazorova L, Avdeef A, Luthman K, Artursson P. Absorption classification of oral drugs based on molecular surface properties. *Journal of Medicinal Chemistry* 2003; **46**:558–570.
9. Dragan A, Read C, Makeyeva E, Milgotina E, Churchill M, Crane-Robinson C, Privalov P. DNA binding and bending by hmg boxes: energetic determinants of specificity. *Journal of Molecular Biology* 2004; **343**:371–393.
10. Jackson R, Sternberg M. DNA binding and bending by HMG boxes: energetic determinants of specificity. *Journal of Molecular Biology* 1995; **250**:258–275.
11. LiCata V, Allewell N. Functionally linked hydration changes in escherichia coli aspartate transcarbamylase and its catalytic subunit. *Biochemistry* 1997; **36**:10161–10167.
12. Raschke T, Tsai J, Levitt M. Quantification of the hydrophobic interaction by simulations of the aggregation of small hydrophobic solutes in water. *Proceedings of the National Academy of Sciences of the United States of America* 2001; **98**:5965–5969.
13. Geng WH, Wei GW. Multiscale molecular dynamics using the matched interface and boundary method. *Journal of Computational Physics* 2011; **230**(2):435–457.
14. Chen D, Wei GW. Quantum dynamics in continuum for proton transport I: basic formulation. *Communications in Computational Physics* 2011. in press.
15. Zheng Q, Chen D, Wei GW. Second-order Poisson–Nernst–Planck solver for ion transport. *Journal of Computational Physics* 2011; **230**:5239–5262.
16. Zheng Q, Wei GW. Poisson–Boltzmann–Nernst–Planck model. *Journal of Chemical Physics* 2011; **134**:194101.
17. Connolly ML. Depth buffer algorithms for molecular modeling. *Journal of Molecular Graphics* 1985; **3**:19–24.
18. Eisenhaber F, Argos P. Improved strategy in analytic surface calculation for molecular systems: handling of singularities and computational efficiency. *Journal of Computational Chemistry* 1993; **14**:1272–1280.
19. Gogonea V, Osawa E. Implementation of solvent effect in molecular mechanics. 1. Model development and analytical algorithm for the solvent - accessible surface area. *Supramolecular Chemistry* 1994; **3**:303–317.
20. Sanner M, Olson A, Spehner J. Reduced surface: an efficient way to compute molecular surfaces. *Biopolymers* 1996; **38**:305–320.
21. Yu Z, Holst M, Cheng Y, McCammon JA. Feature-preserving adaptive mesh generation for molecular shape modeling and simulation. *Journal of Molecular Graphics and Modeling* 2008; **26**:1370–1380.
22. Wei GW, Sun YH, Zhou YC, Feig M. Molecular multiresolution surfaces. *arXiv:mathph/0511001v1*, 2005; 1–11.
23. Zhang Y, Bajaj C, Xu G. Surface smoothing and quality improvement of quadrilateral/hexahedral meshes with geometric flow. *Communications in Numerical Methods in Engineering* 2009; **25**:1–18.
24. Zhang Y, Xu G, Bajaj C. Quality meshing of implicit solvation models of biomolecular structures. *Computer Aided Geometric Design* 2006; **23**(6):510–530.
25. Bates PW, Wei GW, Zhao S. The minimal molecular surface. *arXiv:q-bio/0610038v1*, [q-bio.BM], 2006.
26. Bates PW, Wei GW, Zhao S. The minimal molecular surface. *Midwest Quantitative Biology Conference*, Mission Point Resort, Mackinac Island, MI, September 29–October 1, 2006.
27. Bates PW, Wei GW, Zhao S. Minimal molecular surfaces and their applications. *Journal of Computational Chemistry* 2008; **29**(3):380–391.
28. Bates PW, Chen Z, Sun YH, Wei GW, Zhao S. Geometric and potential driving formation and evolution of biomolecular surfaces. *Journal of Mathematical Biology* 2009; **59**:193–231.
29. Wei GW. Differential geometry based multiscale models. *Bulletin of Mathematical Biology* 2010; **72**:1562–1622.
30. Zheng Q, Chen Z, Wei GW. Variational multiscale models for charge transport I: basic formulation. Submitted, 2011.
31. Chen D, Chen Z, Wei GW. Quantum dynamics in continuum for proton transport II: variational solvent–solute intersurface. *International Journal for Numerical Methods in Biomedical Engineering* 2011. DOI: 10.1002/cnm.1458.
32. Willmore TJ. *Riemannian Geometry*. Oxford University Press: USA, 1997.
33. Osher S, Fedkiw RP. Level set methods: An overview and some recent results. *Journal of Computational Physics* 2001; **169**(2):463–502.
34. Sethian JA. Evolution, implementation, and application of level set and fast marching methods for advancing fronts. *Journal of Computational Physics* 2001; **169**(2):503–555.
35. Sochen N, Kimmel R, Malladi R. A general framework for low level vision. *IEEE Transactions on Image Processing* 1998; **7**(3):310–318.
36. Witkin A. Scale-space filtering: a new approach to multi-scale description. *Proceedings of IEEE International Conference on Acoustic Speech Signal Processing* 1984; **9**:150–153.
37. Perona P, Malik J. Scale-space and edge-detection using anisotropic diffusion. *IEEE Transactions on Pattern Analysis and Machine Intelligence* 1990; **12**(7):629–639.
38. Soltanianzadeh H, Windham JP, Yagle AE. A multidimensional nonlinear edge-preserving filter for magnetic-resonace image-restoration. *IEEE Transactions on Image Processing* 1995; **4**(2):147–161.
39. Wei GW. Generalized Perona–Malik equation for image restoration. *IEEE Signal Processing Letters* 1999; **6**(7):165–167.
40. Wei GW, Jia YQ. Synchronization-based image edge detection. *Europhysics Letters* 2002; **59**(6):814–819.

41. Chan T, Marquina A, Mulet P. High-order total variation-based image restoration. *SIAM Journal on Scientific Computing* 2000; **22**(2):503–516.
42. Osher S, Sethian J. Fronts propagating with curvature-dependent speed: algorithms based on Hamilton–Jacobi formulations. *Journal of Computational Physics* 1988; **79**(1):12–49.
43. Rudin LI, Osher S, Fatemi E. Nonlinear total variation based noise removal algorithms. *Physica D* 1992; **60**(1–4):259–268.
44. Mumford D, Shah J. Optimal approximations by piecewise smooth functions and associated variational problems. *Communications on Pure and Applied Mathematics* 1989; **42**(5):577–685.
45. Blomgren P, Chan T. Color TV: total variation methods for restoration of vector-valued images. *IEEE Transactions on Image Processing* 1998; **7**(3):304–309.
46. Carstensen V, Kimmel R, Sapiro G. Geodesic active contours. *International Journal of Computer Vision* 1997; **22**:61–79.
47. Osher S, Rudin LI. Feature-oriented image enhancement using shock filters. *SIAM Journal on Numerical Analysis* 1990; **27**(4):919–940.
48. Sapiro G, Ringach DL. Anisotropic diffusion of multivalued images with applications to color filtering. *IEEE Transactions on Image Processing* 1996; **5**(11):1582–1586.
49. Chambolle A, Lions PL. Image recovery via total variation minimization and related problems. *Numerische Mathematik* 1997; **76**(2):167–188.
50. Greer JB, Bertozzi AL. H-1 solutions of a class of fourth order nonlinear equations for image processing. *Discrete and Continuous Dynamical Systems* 2004; **10**(1-2):349–366.
51. Greer JB, Bertozzi AL. Traveling wave solutions of fourth order PDEs for image processing. *SIAM Journal on Mathematical Analysis* 2004; **36**(1):38–68.
52. Lysaker M, Lundervold A, Tai XC. Noise removal using fourth-order partial differential equation with application to medical magnetic resonance images in space and time. *IEEE Transactions on Image Processing* 2003; **12**(12):1579–1590.
53. Tasdizen T, Whitaker R, Burchard P, Osher S. Geometric surface processing via normal maps. *ACM Transactions on Graphics* 2003; **22**(4):1012–1033.
54. You Y, Kaveh M. Fourth-order partial differential equations for noise removal. *IEEE Transactions on Image Processing* 2002; **9**(10):1723–1730.
55. Bertozzi AL, Greer JB. Low-curvature image simplifiers: global regularity of smooth solutions and Laplacian limiting schemes. *Communications on Pure and Applied Mathematics* 2004; **57**(6):764–790.
56. Xu M, Zhou SL. Existence and uniqueness of weak solutions for a fourth-order nonlinear parabolic equation. *Journal of Mathematical Analysis and Applications* 2007; **325**(1):636–654.
57. Jin ZM, Yang XP. Strong solutions for the generalized Perona–Malik equation for image restoration. *Nonlinear Analysis—Theory Methods and Applications* 2010; **73**(4):1077–1084.
58. Witelski TP, Bowen M. ADI schemes for higher-order nonlinear diffusion equations. *Applied Numerical Mathematics* 2003; **45**(2–3):331–351.
59. Sun YH, Wu PR, Wei GW, Wang G. Evolution-operator-based single-step method for image processing. *International Journal of Biomedical Imaging* 2006; **83847**:1–27.
60. Wang Y, Wei GW, Yang S-Y. Iterative filtering decomposition based on local spectral evolution kernel. *Journal of Scientific Computing* 2011. DOI: 10.1007/s10915-011-9496-0.
61. Wang Y, Wei GW, Yang S-Y. Mode decomposition evolution equations. *Journal of Scientific Computing* 2011. DOI: 10.1007/s10915-011-9509-z.
62. Wang Y, Wei GW, Yang S-Y. Partial differential equation transform—variational formulation and Fourier analysis. *International Journal for Numerical Methods in Biomedical Engineering* 2011. DOI: 10.1002/cnm.1452.
63. Yang SY, Zhou YC, Wei GW. Comparison of the discrete singular convolution algorithm and the fourier pseudospectral methods for solving partial differential equations. *Computer Physics Communications* 2002; **143**:113–135.
64. Gilboa G, Sochen N, Zeevi YY. Forward-and-backward diffusion processes for adaptive image enhancement and denoising. *IEEE Transactions on Image Processing* 2002; **11**(7):689–703.
65. Gilboa G, Sochen N, Zeevi YY. Image sharpening by flows based on triple well potentials. *Journal of Mathematical Imaging and Vision* 2004; **20**(1–2):121–131.
66. Didas S, Weickert J, Burgeth B. Properties of higher order nonlinear diffusion filtering. *Journal of Mathematical Imaging and Vision* 2009; **35**(3):208–226.
67. Rudin LI, Osher S, Fatemi E. Nonlinear total variation based noise removal algorithms. In *Proceedings of the eleventh annual international conference of the Center for Nonlinear Studies on Experimental mathematics : computational issues in nonlinear science*. Elsevier North-Holland Inc.: Amsterdam, The Netherlands, The Netherlands, 1992; 259–268.
68. Giard J, Macq B. Molecular surface mesh generation by filtering electron density map. *International Journal of Biomedical Imaging* 2010; **2010**(923780):9.
69. Zhang Y, Hubner IA, Arakaki AK, Shakhnovich E, Skolnick J. On the origin and completeness of highly likely single domain protein structures. *Proceedings of the National Academy of Sciences of the United States of America* 2006; **103**:2605–2610.
70. MacKerell Jr AD, Bashford D, Bellott M, Dunbrack Jr RL, Evanseck JD, Field MJ, Fischer S, Gao J, Guo H, Ha S, Joseph-McCarthy D, Kuchnir L, Kuczera K, Lau FTK, Mattos C, Michnick S, Ngo T, Nguyen DT, Prodhom B,

Reiher III WE, Roux B, Schlenkrich M, Smith JC, Stote R, Straub J, Watanabe M, Wiorkiewicz-Kuczera J, Yin D, Karplus M. All-atom empirical potential for molecular modeling and dynamics studies of proteins. *Journal of Physical Chemistry B* 1998; **102**(18):3586–3616.

71. Dolinsky TJ, Nielsen JE, McCammon JA, Baker NA. PDB2PQR: an automated pipeline for the setup, execution, and analysis of Poisson–Boltzmann electrostatics calculations. *Nucleic Acids Research* 2004; **32**(S2):W665–W667.

72. Zhou YC, Feig M, Wei GW. Highly accurate biomolecular electrostatics in continuum dielectric environments. *Journal of Computational Chemistry* 2008; **29**:87–97.

73. Geng WH, Yu SN, Wei GW. Treatment of charge singularities in implicit solvent models. *Journal of Chemical Physics* 2007; **127**:114106.

74. Bhat S, Purisima EO. Molecular surface generation using a variable-radius solvent probe. *Proteins: Structure, Function, and Bioinformatics* 2006; **62**:244–261.

75. Chen D, Chen Z, Chen CJ, Geng WH, Wei GW. MIBPB: a software package for electrostatic analysis. *Journal of Computational Chemistry* 2011; **32**:657–670.

76. Yu SN, Geng WH, Wei GW. Treatment of geometric singularities in implicit solvent models. *Journal of Chemical Physics* 2007; **126**:244108.

77. Chern IL, Liu J-G, Weng W-C. Accurate evaluation of electrostatics for macromolecules in solution. *Methods and Applications of Analysis* 2003; **10**(2):309–328.

78. Yu SN, Wei GW. Three-dimensional matched interface and boundary (MIB) method for treating geometric singularities. *Journal of Computational Physics* 2007; **227**:602–632.

79. Yu SN, Zhou YC, Wei GW. Matched interface and boundary (MIB) method for elliptic problems with sharp-edged interfaces. *Journal of Computational Physics* 2007; **224**(2):729–756.

80. Zhao S, Wei GW. High-order FDTD methods via derivative matching for Maxwell's equations with material interfaces. *Journal of Computational Physics* 2004; **200**(1):60–103.

81. Zhou YC, Wei GW. On the fictitious-domain and interpolation formulations of the matched interface and boundary (MIB) method. *Journal of Computational Physics* 2006; **219**(1):228–246.

82. Zhou YC, Zhao S, Feig M, Wei GW. High order matched interface and boundary method for elliptic equations with discontinuous coefficients and singular sources. *Journal of Computational Physics* 2006; **213**(1):1–30.

83. Chen CJ, Saxena R, Wei GW. Differential geometry based multiscale models for virus formation and evolution. *International Journal of Biomedical Imaging* 2010; **2010**(308627):1–9.

84. Lawson CL, Dutta S, Westbrook JD, Henrick K, Berman HM. Representation of viruses in the remediated PDB archive. *Acta Crystallographica Section D- Biological Crystalography* 2008; **64**:874–882.